Accepted 28 July 2025 – Pure & Applied Geophysics

Complex Love numbers in the diurnal and semidiurnal tidal bands determined from satellite tracking and altimetry

R. D. Ray[1], B. D. Loomis[1], K. E. Rachlin[1,2], J. J. Otero Torres[3]

[1]NASA Goddard Space Flight Center, Greenbelt, USA.
[2]KBRwyle, Greenbelt, USA.
[3]National Geospatial-Intelligence Agency, Springfield, USA.

Contributing authors: richard.ray@nasa.gov; bryant.d.loomis@nasa.gov; kenneth.e.rachlin@nasa.gov; jason.j.oterotorres@nga.mil;

Abstract

New tidal solutions from laser tracking of eight geodetic satellites and from a constellation of radar altimeters are combined to determine the complex Love number k_2 for four lunar tidal constituents in the diurnal and semidiurnal bands. The tidal solutions for each data type must account for inconsistent prior Love numbers; the altimetry community has historically used elastic Love numbers. Use of the complex Love numbers recommended by current international conventions results in a small (order 4‰) discrepancy between altimeter and tracking solutions for the degree-2 prograde spherical harmonics; this points to an anelastic Earth model that is too dissipative, with a phase lag slightly too large. Our estimated phase lag for k_2 varies slightly across the tidal bands, from $0.228° \pm 0.024°$ for O_1 to a smaller $0.178° \pm 0.020°$ for M_2, with corresponding tidal Q rising from 250 to 320. Results for N_2 and Q_1 are consistent, but with much larger uncertainties. There is some interdependence on the values adopted for other Love and loading numbers, which we account for. A possibly important systematic error arises from seawater density, needed to relate ocean tidal elevations to gravitational Stokes coefficients. A constant mean density of 1035 kg m^{-3} is used, but allowance for spatial variations in ocean density may be necessary.

Keywords: Tides, Love number, Satellite geodesy, Tidal Q

1 Introduction

Tidal studies have been an important part of satellite geodesy almost since the beginning of the satellite era (e.g., Kaula 1962; Kozai 1968; Smith et al. 1973). Tracking by satellite laser ranging (SLR) has proven especially valuable for determining the important spherical harmonic components of degree 2, terms that completely describe quantities related to global tidal energetics and external rotational torques (Lambeck 1977). Nonetheless, as a tool for investigating tides, SLR tracking has been overshadowed by satellite altimetry, since altimetry is capable of fine-scale ocean mapping (e.g., Le Provost 2001), leading to accurate global cotidal maps (Stammer et al. 2014). Even the resulting low-degree spherical harmonics from altimetry, found by numerical quadrature of global maps (e.g., Egbert and Ray 2001), obtain precisions nearly comparable to those of SLR solutions.

Yet neither satellite tracking nor satellite altimetry alone can separate earth tides from ocean tides. The two in combination can, however, as tides affect each data type in different ways in terms of geopotential and geometry. Such a combination has previously been used to determine the imaginary part of the complex

Love number k_2 at the M_2 frequency, or the phase lag in the body tide, and thus the corresponding tidal Q and body-tide dissipation rate (Ray et al. 1996, 2001). The present paper is a long overdue update to that work. It improves the precision of both real and imaginary components of k_2 and extends the analysis to other major lunar constituents in the diurnal and semidiurnal bands.

The analysis here relies on new tidal solutions from both tracking and altimetry. These are described in Sections 3 and 4, respectively. Section 5 lays out the approach to determine k_2 which is based on a small systematic difference between the altimeter and tracking tidal solutions. Such differences can also arise from inconsistencies in formulation of tidal parameterizations or in geophysical constants, so it is critical that these be minimized to the extent possible. Careful assessment of uncertainties is necessary to establish that small differences between tracking and altimeter coefficients are truly due to real geophysical processes.

The method is applied to tidal solutions for four constituents, listed in Table 1. Only lunar tides are considered; solar tides are more difficult to handle owing to the confounding effects of atmospheric tides. Atmospheric tides also affect our analysis of lunar tides, of course, and these are accounted for below and described in detail in Appendix A. However, lunar atmospheric tides are much smaller and less complicated than solar tides, as solar tides are forced by both gravitation and insolation, as well as by boundary heating and thermodynamics (Schindelegger et al. 2023). These complexities are avoided here by focusing on lunar tides alone.

2 Love numbers

The Love numbers k_n, h_n, l_n—associated with the potential, vertical displacement, and horizontal displacement, respectively—and similar loading numbers k'_n, h'_n, l'_n permeate all geodetic discussions of tides (Melchior 1966; Lambeck 1988). Their importance lies in the information they reveal about the Earth's interior, most notably because they refer to frequencies outside the seismic band. Our goal here is to use satellite measurements to place constraints on k_2, given loose constraints on the other numbers.

The Love number k_n relates the primary tidal potential Φ^P_n of spherical harmonic degree n to the secondary potential induced by the body tide: $\Phi^S_{B,n} = k_n \Phi^P_n$. Modern developments of the tidal potential have been extending to ever higher n; Hartmann and Wenzel (1995) take their expansion to degree 6. In our modeling of satellite orbit perturbations, we use $n = 2, 3$ potentials, but our focus is on those tides of Table 1, which are of degree 2. With k_2 complex, the body tide phase lag, which gives important insight into tidal dissipation, is given by $\epsilon = -\arg k_2$. The effective $Q = 1/\tan\epsilon$. How this Q may relate to attenuation and the inherent Q of the mantle is discussed by Lau et al. (2017).

Data processing for both satellite tracking and satellite altimetry employs all six of the above-listed Love and loading numbers, with h_2, h'_n employed in altimetry to correct the altimeter ranges for the solid tide, with h_2, l_2, h'_n, l'_n employed in both systems for modeling the motion of tracking stations, and with k_2, k'_n employed in both for modeling satellite dynamics. Our combined analysis of tracking and altimeter-derived tides thus rests on the adoption of prior values for these constants. We endeavor to account for any dependence of the estimated k_2 on these prior values.

The 2010 Conventions of the International Earth Rotation and Reference Systems Service (IERS) (Petit et al. 2010) recommend for k_2 the complex values listed in Table 1. The implied phase lag is $\epsilon = 0.247°$ for M_2 and $0.264°$ for O_1. Our conclusions below suggest that these phase lags are slightly too large.

3 Tides from Satellite Tracking

We have derived a suite of new tidal solutions using SLR tracking of the eight geodetic satellites listed in Table 2 and pictured in Figure 1. Each estimated tidal constituent has been parameterized as an ocean tide elevation, ζ, determined after using prior (but imperfect) models of the body tide and atmospheric tide. We are here interested in only one spherical harmonic component of ζ: the prograde wave of degree $n = 2$ and order m equal to the tidal species—1 for diurnal constituents, 2 for semidiurnal—which is the same degree/order as the forcing potential. The component is written

$$\zeta^+_{nm}(\theta, \varphi, t) = D^+_{nm} \cos\left(\Theta(t) + m\varphi - \psi^+_{nm}\right) P^m_n(\cos\theta) \tag{1}$$

where $P^m_n(\mu)$ is an unnormalized associated Legendre function and the argument $\Theta(t)$, given in Table 1, is the standard Doodson argument as used in oceanography. The form of (1) is consistent with that used in a number of previous works that study tidal energetics

Table 1 Tidal constituents analyzed

Tide	Doodson no.	Argument $\Theta(t)$	Frequency (°/h)	$\bar{H}$ (mm)[1]	Prior[2] k_2
Q_1	135.655	$\tau - 2s + p - \pi/2$	13.398661	12.925	$0.29784 - i0.00139$
O_1	145.555	$\tau - s - \pi/2$	13.943036	67.513	$0.29747 - i0.00137$
N_2	245.655	$2\tau - s + p$	28.439730	15.578	$0.30102 - i0.00130$
M_2	255.555	2τ	28.984104	81.367	$0.30102 - i0.00130$

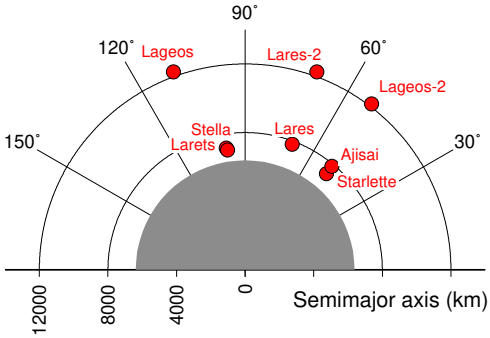

Fig. 1 Semimajor axes and inclinations of the eight geodetic satellites used for tracking-based ocean tide solutions. Laser ranging data to these satellites were provided by, and partially processed by, the International Laser Ranging Service (Pearlman et al. 2019).

(e.g., Egbert and Ray 2001). The form used in our orbit codes is only slightly different:

$$\zeta^+_{nm}(\theta,\varphi,t) = \left[A^+_{nm}\cos(\Theta(t)+m\varphi) + B^+_{nm}\sin(\Theta(t)+m\varphi)\right]\bar{P}^m_n(\cos\theta) \quad (2)$$

where A^+_{nm}, B^+_{nm} are now in-phase and quadrature elevation coefficients and $\bar{P}^m_n(\mu)$ is a Legendre function normalized as in Heiskanen and Moritz (1967). Our orbit codes internally convert the elevation coefficients to tidally varying Stokes coefficients (cf. Petit et al. 2010, Eq. (6.21)):

$$\{C,S\}^+_{nm} = \{A,B\}^+_{nm}\,\frac{4\pi G\rho_w}{g}\left(\frac{1+k'_n}{2n+1}\right), \quad (3)$$

where G is the Newtonian constant, g is gravitational acceleration, ρ_w is the density of seawater, and k'_n are loading Love numbers. These constants have some bearing on our final results; they are discussed below.

3.1 SLR Background Modeling

The background modeling required for the analysis of SLR is important in general, and for the tide solutions several of the background models are critical to our combined SLR/altimeter analysis of Section 5.

Table 2 Geodetic satellites used in this work.

Satellite	Launch date	Altitude[1]	Inclination
Starlette	1975	812	49.8°
LAGEOS-1	1976	5838	109.8°
Ajisai	1986	1485	50.0°
LAGEOS-2	1992	5617	52.6°
Stella	1993	804	98.7°
Larets	2003	690	98.2°
LARES-1	2012	1437	69.5°
LARES-2	2022	5900	70.2°

[1]Altitude given is perigee, in km.

3.1.1 Geophysical constants

Eq. (3) requires a number of constants for the conversion between ocean tide elevations and the Stokes coefficients used for computing satellite dynamics. The equation can be expressed in terms of other constants—e.g., the mass M of the earth can replace g in different ways, but each expression requires adoption of similar kinds of constants. For (3) the important ones are as follows:

- The Newtonian constant is set to 6.672×10^{-11} $m^3\,kg^{-1}\,s^{-2}$. This was the accepted value of G circa 1973, but most experimental determinations since then have been slightly higher; CODATA[1] (Committee on Data for Science and Technology) now recommends 6.6743. However, a fairly recent measurement by atom interferometry (Rosi et al. 2014) gives 6.6719, close to our adopted value.
- The gravity acceleration g is here set to $9.820\ m\,s^{-2}$, which is equivalent to GM/R^2 where R is the mean radius of the earth. The equivalent IERS expression uses g_e, the equatorial acceleration, which is generally interpreted to include a term arising from the centrifugal acceleration and another term from the dynamical flattening J_2, giving a total value approximately $9.780\ m\,s^{-2}$ (Groten 2004). These additional accelerations are unwarranted in the present context. Other authors (e.g. Cheng et al. 1992) have used

[1]https://pml.nist.gov/cuu/Constants, accessed 14 April 2025.

GM/a^2 with a the equatorial radius, or 9.798 m s^{-2}. The difference from our value, about 0.2%, is within our final k_2 uncertainty limits.

- The loading Love numbers k'_n are based on Farrell (1972). These are real numbers, i.e., they assume an elastic earth. Any error arising from this assumption will be accounted for below.
- The mean seawater density ρ_w is set to 1035 kg m^{-3} (Gill 1982). The value recommended by the IERS is 1025 kg m^{-3}, which is incorrect, as that value is closer to the density of water at the surface. Since the ocean tide at any location is a result of convergence and divergence of water throughout the whole water column (as reflected in the equation of continuity), use of the surface density is inappropriate. To check this value, we have computed mean water-column ocean densities from the temperature and salinity data of the 2013 World Ocean Atlas and found a global average of 1035.6, close to Gill's value. Recent work with GRACE suggests that it may be necessary to account for the water-column density as a function of location (Han et al. 2020), which requires combining the seawater density with tidal elevation in the spherical harmonics. We have not followed through with that here, as doing so will require some reformulation, including of Eq. (3), in addition to incorporation of density into integrals for the altimeter-derived spherical harmonics. Note that for M_2 the surface integral $\iint \zeta \rho_w Y_2^2 \, dA$ yields a value for $D_{22}^+ \sin\psi_{22^+}$ approximately 0.3% larger than if ρ_w is taken as a constant, so possibly a simple constant density near 1035 kg m^{-3} is sufficiently accurate in light of other error sources.

Several of these constants are used directly in Eq. (3) to scale the geopotential to tidal elevation. Thus, for example, a 1% error in seawater density ρ_w leads to a 1% error in our estimate of D_{nm}^+, which would be a significant error.

3.1.2 Body tides

For our prior model of the body tides, we have followed the 2010 IERS Conventions (Petit et al. 2010), which recommend the k_2 Love numbers listed in Table 1. This choice is not critical, but it does affect how the SLR and altimeter solutions are combined; see details in Section 5.

3.1.3 Non-tidal atmosphere/ocean model

We have employed the models developed at GFZ, Potsdam, for use by the GRACE project teams—the so-called AOD1B models (Release 7). These gravitational models remove variance associated with non-tidal atmospheric and oceanic mass movements. They are in the form of a spherical harmonic series to $N = 180$, with a 3-hour time-step. Details are given by Shihora et al. (2022).

To our knowledge no previous SLR tide inversion has employed this kind of background model. It is likely beneficial because of the way tides are aliased to very low frequencies in the satellite observations (Lambeck 1988). Those frequencies are generally dominated by atmospheric and oceanic variability, which has a typically red spectrum, so the lower the tidal alias frequency the worse the potential non-tidal contamination of our tide estimates. The use of the GFZ model should reduce this contamination.

3.1.4 Atmospheric tides

To isolate the ocean tide in the SLR data, we must rely on forward models of the atmospheric tide. For this we have extracted the M_2 barometric tide from the European Centre for Medium-range Weather Forecasts (ECMWF) reanalysis product ERA5 (Hersbach et al. 2020) for years 2006–2022. Subsequently, we have seen evidence that the ERA5 tides are not sufficiently accurate (e.g., Figure A2 below). We have therefore adjusted our SLR solutions to agree with the empirically derived M_2 air tide of Schindelegger and Dobslaw (2016). Details of this, and how the air tide is made more consistent with the non-tidal GFZ model, are discussed in Appendix A.

3.1.5 SLR station displacements

In theory the ocean tides dynamically estimated from orbit perturbations could be impacted by errors in the tidal displacement models applied to the SLR tracking stations, both from the body tide (h_2, l_2) and from ocean tide loading (h'_n, l'_n). The latter were here based on the GOT4.10c ocean tide model, using the computational package of Agnew (2013); the former were based on the IERS body-tide model. It is generally thought that ocean-tide loading errors cannot significantly affect computed satellite orbits because these appear as rapid (but false) perturbations in range that cannot by easily accommodated by dynamically integrated orbits. Errors in body-tide displacements vary

more slowly with the satellite orbit plane and are less easily dismissed. However, we have explicitly tested the latter and found that the impact on the SLR tidal solutions is minimal; see below.

Tidal geocenter motion was also accounted for with the same GOT4.10c ocean-tide model. We have also checked for dependence of our solution on geocenter motion, and it too is minimal; again see below.

3.2 SLR Tide Estimates

Using SLR tracking of the eight geodetic satellites shown in Figure 1, we have derived a suite of new tidal solutions D^+_{nm}, ψ^+_{nm} for each of 24 constituents. Here we discuss only those aspects relevant to the determination of k_2 for the four lunar tides of Table 1, as details of the full SLR solutions will be given elsewhere. In brief summary, the solutions were computed from data collected by the international laser ranging network (Pearlman et al. 2019) over the period 1994–2023. Normal equations were constructed for prograde spherical harmonic coefficients of degrees $n = 2, 3, \ldots, 6$ and order m equal to the tidal species, which are the only coefficients that lead to long-period perturbations in orbit parameters (Lambeck 1988). The data were processed in 7-day arcs, consistent with the procedures applied for estimation of low-degree time-variable gravity coefficients by Loomis et al. (2020).

As usual, nodal modulations of the lunar tides were accounted for at the observation level by standard methods (Pugh and Woodworth 2014). We have extended this formalism to account also for modulations from minor constituents not explicitly estimated. Thus, for example, the estimate of Q_1 accounts for the presence of ρ_1, and the estimate of M_2 accounts for the presence of $\alpha_2, \beta_2, \Gamma_2, \delta_2$, and so forth. This essentially implies estimation of tidal "groups" rather than tidal "constituents," with an assumed constant admittance within each tidal group. Any climate-induced seasonal modulations were ignored.

To test the robustness of the tidal solutions we have computed three solutions: (1) as described above, (2) with only $n = 2$ coefficients estimated, and (3) with only SLR data from 2000–2023 used. Solution (2) explicitly tests for potential problems associated with correlations between degrees 2 and the higher even degrees, which are often observed in SLR analyses of $J_2, J_4, \ldots$ (Smith 1965; Tucker et al. 2022). The results for each of these three solutions are tabulated in Table 3.

Table 3 Estimated Degree-2 Prograde Tidal Coefficients from SLR.

Tide	Solution	A^+_{2m} (meters)	B^+_{2m} (meters)	D^+_{2m} (mm)	ψ^+_{2m} (deg)	σ (mm)
Q_1	1	-3.1548E-03	3.0989E-03	5.709	135.51°	0.048
	2	-3.1835E-03	3.0769E-03	5.716	135.98°	0.044
	3	-3.1471E-03	3.0964E-03	5.700	135.46°	0.051
O_1	1	-1.4003E-02	1.3577E-02	25.179	135.88°	0.042
	2	-1.3962E-02	1.3510E-02	25.082	135.94°	0.039
	3	-1.4008E-02	1.3579E-02	25.186	135.89°	0.044
N_2	1	-5.2794E-03	9.2377E-03	6.868	119.75°	0.020
	2	-5.2810E-03	9.2395E-03	6.870	119.75°	0.020
	3	-5.2782E-03	9.2235E-03	6.860	119.78°	0.022
M_2	1	-3.0763E-02	3.7835E-02	31.476	129.11°	0.017
	2	-3.0779E-02	3.7836E-02	31.483	129.13°	0.017
	3	-3.0750E-02	3.7816E-02	31.462	129.12°	0.018

Solution 1 should be considered the primary tide solutions.

A glance at Table 3 shows that the given 1σ error estimates are reasonably consistent with the variability in the three solutions. For example, for the large M_2 coefficients, the amplitudes differ by 0.021 mm or less, and the phases (in radians after scaling by D^+_{22}) differ by 0.011 mm, both roughly consistent with a 1σ uncertainty of 0.017 mm. Most of the constituents also show only small differences between Solutions 1 and 2, indicating no significant even-degree correlation problems. An exception is the small J_1 constituent (not shown) for which the Solution-2 phase is offset by an amount that exceeds 2σ.

As another check on the estimated uncertainties of the coefficients, we have also solved for mean monthly coefficients for M_2; see Figure 2. The spread among these monthly solutions is expected to be of order $\sqrt{12}$ larger than the errors given in the table, or about 0.06 mm. (Actually, using the spread in these monthly solutions may be too pessimistic as an assessment of σ, because there is some evidence that the monthly solutions contain real signal arising from seasonal variations in M_2.) The standard deviation of the monthly solutions shown in Figure 2 is about 0.08 mm, only slightly larger than 0.06 mm, again suggesting that the σ values of Table 3 are realistic.

Although not investigated nor described here in detail, we have computed two more inversions to test modeling sensitivities. In the first, simultaneous tidal geocenter parameters have also been estimated. Of the constituents in Table 1, geocenter motion is the largest for the diurnal O_1. The resulting solution for (D^+_{21}, ψ^+_{21}) was (25.197 mm, 135.93°), which agrees

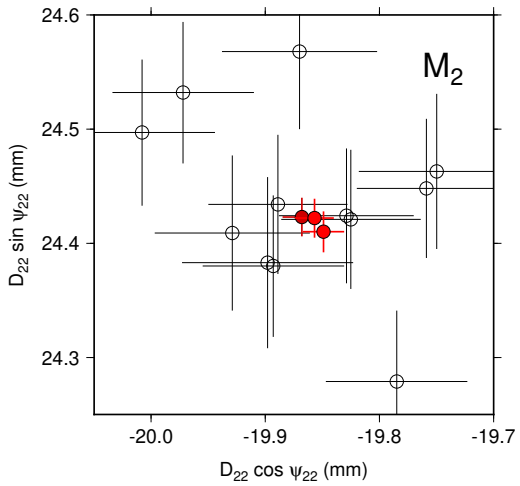

Fig. 2 SLR solutions for the in-phase and quadrature coefficients of the M_2 ocean tide. Red symbols correspond to the three SLR solutions in Table 3; 12 black open circles correspond to monthly mean solutions.

with the above solutions well within the standard error of 0.042 mm. Errors arising from inaccurate geocenter modeling are therefore probably minimal.

Finally, we tested dependence on errors of the prior h_2 used to model SLR station displacements. This was done by purposely setting h_2 to 0.55, a (large) 10% error. Yet the effect on the M_2 ocean-tide solution was only 0.01 mm, and thus insignificant. For reasons unclear, the effect on O_1 was much larger, about 0.1 mm, all in the in-phase component. Thus, even with this inordinately large error in modeling the motion of tracking stations, there would be only a small impact on estimates of $|k_2|$ and essentially no impact on estimates of the phase lag ϵ.

4 Tides from Satellite Altimetry

This section can be far briefer than the previous section, as we simply adopt some previous altimeter tide solutions that are documented elsewhere. Our main altimeter-based model is GOT5.5 (Ray 2025), with comparisons made with GOT4.10c (Ray 2013), FES2014 (Lyard et al. 2021), and FES2022 (F. Lyard, pers. comm.). All of these are global models on high-resolution grids, based on decades of multi-mission altimetry. Spherical harmonic coefficients were computed while accounting for the earth's ellipsoidal shape (Han et al. 2020), which affects degree-2 coefficients at about the level of 0.3%, similar to the earth's flattening. The relevant coefficients for GOT5.5 are tabulated in Table 4.

Table 4 Degree-2 Prograde Tidal Coefficients from Altimeter Model GOT5.5.

Tide	D^+_{2m}	ψ^+_{2m}	σ^1
Q_1	5.893	136.37°	0.04
O_1	26.205	137.30°	0.06
N_2	7.019	120.82°	0.03
M_2	32.350	129.77°	0.06

$m = 1$ for diurnal tides; $m = 2$ for semidiurnals. Amplitude units are mm.

[1]Standard error σ, in mm, is determined from the scatter of four altimeter solutions.

A critical point concerns the body tide correction used by the present-day altimeter community, including during the development of the four tide models used here. The correction has not been consistent with IERS recommendations but instead continues to follow a convention adopted for the early Geosat mission. Except for adjustments near K_1, this old convention uses for all constituents a constant Love number $h_2 = 0.609$, taken from Wahr's elastic model for the semidiurnal band (Wahr 1981). The inconsistency of body tide models for tracking and altimetry is addressed in the following section.

Less critical, but still worth noting, is the modeling used for solid-earth load tides. For the two GOT models, the load tides were computed iteratively as part of the ocean-tide solutions. These used h'_n elastic loading numbers from Farrell (1972), aside from the degree-1 coefficients which followed Desai and Ray (2014). In particular, $h'_2 = -1.001$. For the FES models, a nearly equivalent value was used: $h'_2 = -0.99158$ (Jean-Paul Boy, pers. comm., April 2025).

The degree-2 prograde coefficients for the four ocean-tide models for M_2 are plotted in Figure 3a. Error estimates for these coefficients are unavailable, so as a proxy for that we use the scatter in this figure. The vector standard deviation for these four models for M_2 is 0.06 mm. Uncertainties for the other constituents are listed in Table 4.

5 Combined Analysis of Tracking and Altimeter Solutions

The notation and much of the approach that follows builds on our previous work (Ray et al. 2001). The approach can be briefly summarized. The main idea is to examine the secondary potential that is induced by the tidal deformations of the solid and fluid tides, which

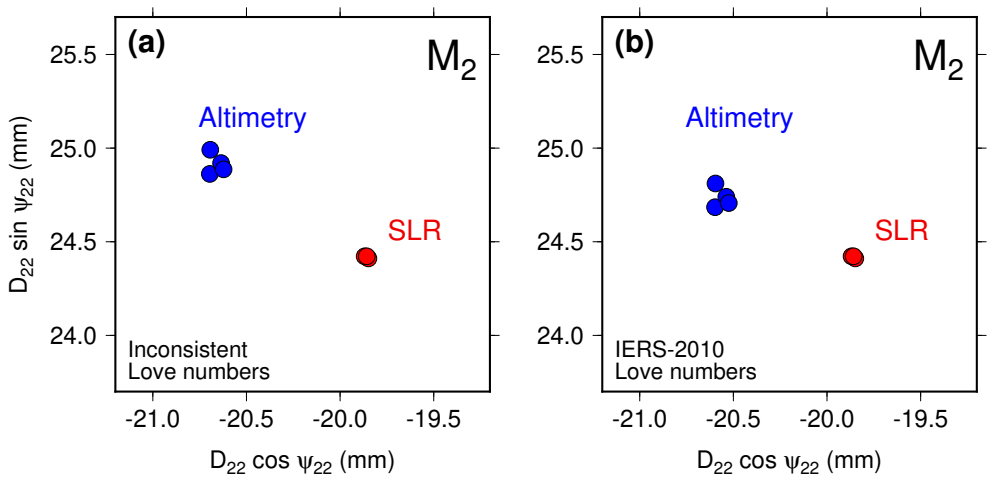

Fig. 3 Prograde M_2 coefficients for (blue) four altimeter tide models and (red) three, mostly overlapping, SLR solutions from Table 3. Two panels show dependence on prior Love numbers for each type of analysis. (a) Altimeter Love number $h_2 = 0.609$ (Wahr 1981); SLR Love number $k_2 = 0.30102 - i0.00130$ (IERS). (b) Altimeter Love number $h_2 = 0.60780 - i0.00220$; SLR Love number $k_2 = 0.30102 - i0.00130$, both from IERS. Panel (b) indicates that the 2010 IERS Love numbers are inconsistent with the SLR and altimeter observations.

in a sense are directly observed by the tracking data after accounting for the primary potential, and which may also be computed from altimeter solutions. Systematic discrepancies between altimetry and tracking allows observational constraints to be placed on k_2. We now drop all subscripts and superscripts on D^+_{22}, ψ^+_{22}, but add superscripts T or A to denote Tracking or Altimetry solutions, respectively.

The primary astronomical potential, written in a form consistent with Eq. (1) is (Cartwright and Tayler 1971)

$$\Phi^P(\theta,\varphi,t) = g\bar{H}\, P_2^m(\cos\theta)\, \cos\left(\Theta(t) + m\varphi\right) \quad (4)$$

where $\bar{H}$ is an equilibrium tidal amplitude (potential divided by g) as extracted from the tables of Cartwright and Edden (1973) and given in Table 1.

The secondary potential Φ^S, induced as a response to the primary, can be decomposed into three components:

$$\Phi^S = \Phi^S_B + \Phi^S_{O+L} + \Phi^S_{A+L}, \quad (5)$$

arising from the body tide, the ocean tide and its load, and the atmospheric tide and its load. We will drop the atmospheric component under the assumption that it is sufficiently small to ignore or that the SLR data have been adequately corrected for it (see Appendix A).

We write all potentials in the form

$$\Phi(\theta,\varphi,t) = \mathrm{Re}[\hat{\Phi}\, P_2^m(\cos\theta)\, e^{i(\Theta(t)+m\varphi)}] \quad (6)$$

where $\hat{\Phi}$ is a complex amplitude exclusive of P_2^m. Thus, the primary potential amplitude simplifies to $\hat{\Phi}^P = g\bar{H}$. Corresponding expressions for the secondary potential amplitudes are

$$\hat{\Phi}^S_B = g\bar{H}k \quad (7)$$

$$\hat{\Phi}^S_{O+L} = \alpha g(1+k')De^{-i\psi} \quad (8)$$

where k, k' are possibly complex, the constant $\alpha = (3\rho_w/5\rho_e) = 0.1126$, and (D,ψ) are coefficients of the true (not estimated) tide. These must be related to what is actually determined in the SLR and altimetry analyses.

In the SLR analyses, orbit perturbations are used to solve essentially for the secondary potential $\hat{\Phi}^S$, which is normally parameterized as an (elastic or anelastic) body tide and a residual ocean tide and its crustal loading (generally elastic):

$$\hat{\Phi}^S = k_o g\bar{H} + \alpha g(1+k'_o)D^T e^{-i\psi^T} \quad (9)$$

where the o subscripts refer to the adopted prior values of the relevant Love numbers.

Altimetry aims to directly measure ζ, but its measurements are in error owing to errors in the adopted values of Love number h and loading number h'. That is, the altimetry gives

$$D^A e^{-i\psi^A} = De^{-i\psi} + (h-h_o)\bar{H} + \alpha(h'-h'_o)De^{-i\psi}. \quad (10)$$

Eqns. (7, 9, 10), relating observations and tide parameterizations, prove useful in the following section.

5.1 Adjustment of tidal coefficients for inconsistent priors

In our combined tracking-altimeter analysis for k_2, it is critical that allowance is made for any inconsistent prior models of body tides, and potentially other constants as well. Part of the discrepancy between altimetry and SLR rests with these prior models. It is not mandatory that body-tide models be consistent, but it simplifies matters to make them so. An adjustment of the estimated tide coefficients for a different prior can be done easily.

From (10) a change in the displacement Love number $\Delta h = h_{\rm new} - h_{\rm old}$ leads to a simple trade-off with the altimeter-estimated coefficients:

$$\text{Adjusted } D^A e^{-i\psi^A} = \text{Original } D^A e^{-i\psi^A} - \Delta h\, \bar{H}. \tag{11}$$

This has been used to adjust the altimeter coefficients, shown in Figure 3a, replacing Wahr's Love number h as currently used by the altimeter community with the (complex) 2010 IERS Conventions value, to be more consistent with the k Love number used in the tracking solutions. Figure 3b shows the adjusted coefficients. The adjustment is small, as the altimeter cluster is seen to move only slightly.

An important conclusion to draw from Figure 3b is that the anelastic Love numbers, h and k, as recommended by the 2010 IERS Conventions for M_2 are inconsistent with the altimeter and tracking observations.

To simplify the analysis below, rather than adjusting the altimeter coefficients, we prefer to adjust the tracking coefficients so that, like the original altimeter coefficients, they are based on a purely elastic k value. For this we used the values $k = 0.302$ for semidiurnal tides, $k = 0.298$ for the two diurnal tides, again taken from Wahr (1981). From (9) a change in the Love number Δk leads to an adjusted set of coefficients

$$\text{Adjusted } D^T e^{-i\psi^T} = \text{Original } D^T e^{-i\psi^T} - \Delta k\, \bar{H}[\alpha(1+k')]^{-1}. \tag{12}$$

The M_2 adjusted coefficients are shown in Figure 4a. Clearly the tracking tide solution is far more sensitive to the body tide Love numbers than is the altimeter solution, since this figure differs substantially from Figures 3a,b. Figure 4 shows similar diagrams for the other lunar constituents of interest. All display a similar pattern with the cluster of SLR coefficients sitting displaced from the cluster of altimeter points, with the offset mainly in the quadrature direction.

5.2 Combined constraints on k_2: Approach

Accounting for certain errors in our prior Love and loading numbers k_o, k'_o, we may use Eq. (9) to write the tidal coefficients $De^{-i\psi}$ in terms of the estimated tracking solution, and we may use Eq. (10) to write a similar expression in terms of the altimeter solution. Equating the two gives

$$\left(\frac{1+k'_o}{1+k'}\right) D^T e^{-i\psi^T} - \frac{(k-k_o)\bar{H}}{\alpha(1+k')} = \left[D^A e^{-i\psi^A} - (h-h_o)\bar{H}\right]\left[1+\alpha(h'-h'_o)\right]^{-1}. \tag{13}$$

We use (13) below to solve for k, but it is first enlightening to simplify this equation by noting that the first factor $(1+k'_o)/(1+k') \approx 1$ and similarly the last factor $(1+\alpha\Delta h') \approx 1$. Dropping those two factors gives

$$D^T e^{i\psi^T} - D^A e^{i\psi^A} = (k-k_o)\frac{\bar{H}}{\alpha(1+k')} - (h-h_o)\bar{H}, \tag{14}$$

giving the difference between the tracking and altimeter tide solutions as a balance between errors in our two priors for k and h. The factor that scales k is much larger than the factor scaling h, since $1/(\alpha(1+k')) \approx 13$. This statement is consistent with the previous discussion in Section 5.1 in which changes of Love number had a much larger effect on the tracking solution than the altimeter solution. The important conclusion is that the combination of altimeter and tracking tide solutions sets far tighter constraints on k than on h. We can thus solve for k from these tide differences, and the error in the other Love or loading numbers adds only a small uncertainty, which can be accounted for. Moreover, if the priors k_o, h_o are real, as they are in Figure 4, then the large out-of-phase differences $(D^T \sin\psi^T - D^A \sin\psi^A)$ seen in the figure determine the imaginary part of k. The much smaller in-phase differences $(D^T \cos\psi^T - D^A \cos\psi^A)$ lead to small adjustments to the real part of k.

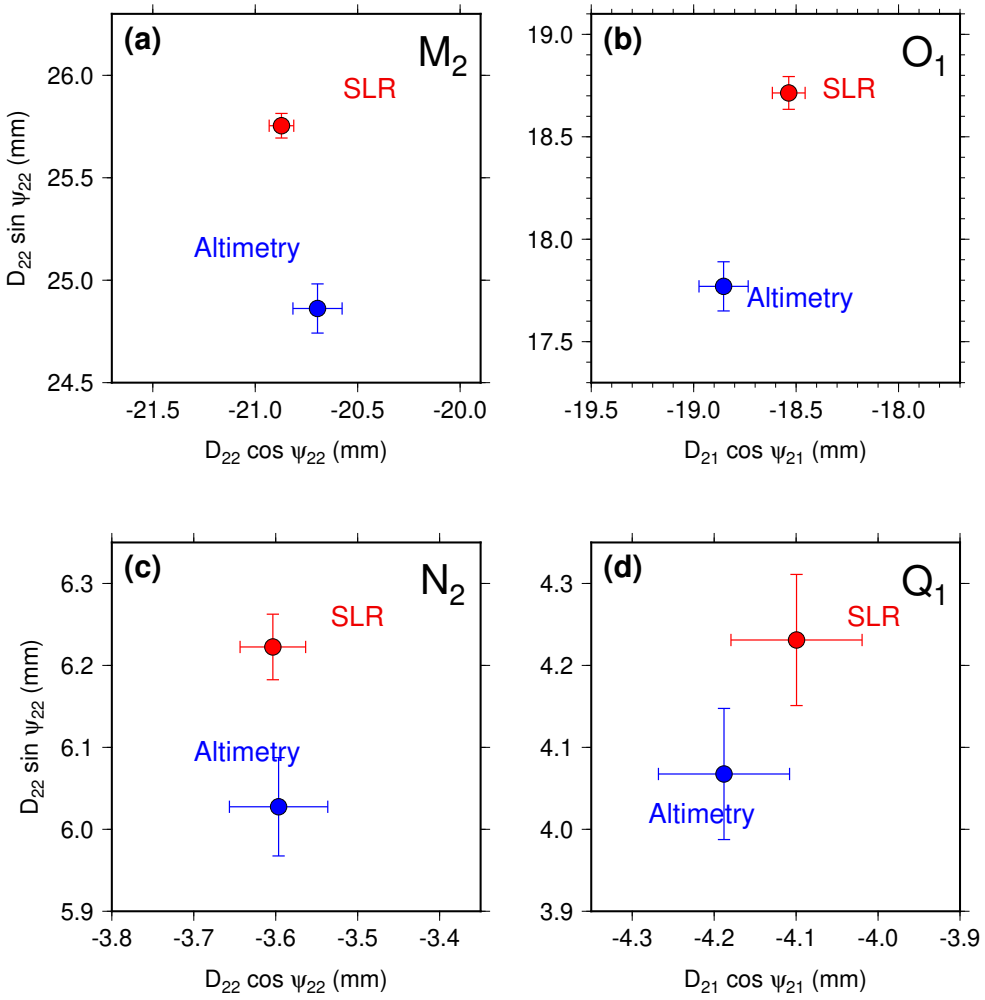

Fig. 4 Prograde M_2 coefficients for (blue) GOT5.5 altimeter tide model and (red) SLR solution 1 from Table 3. Both altimeter and SLR coefficients have been adjusted to use prior elastic body-tide parameters from Wahr (1981). Note change in scale for different panels. Plotted error bars are here 2σ (unlike other figures) to make more legible.

Another simplification of (13) was employed by Ray et al. (2001) by assuming the phase lags in the tidal displacement and in the induced secondary potential are approximately equal, i.e., that $\epsilon = -\arg k = -\arg h$. Using only the quadrature component of the tracking and altimeter tide differences then gives

$$\epsilon = (D^T \sin\psi^T - D^A \sin\psi^A) \frac{\alpha(1+k')}{\bar{H}(k_o - h_o\alpha(1+k'))} \tag{15}$$

which is equivalent to Eq. (15) of Ray et al. (2001). However, the displacement and potential phase lags need not be identical. For example, the IERS Love numbers give a ratio $\arg k/\arg h = 1.19$ for M_2, and 1.11 for O_1. Of the suite of 19 Earth models developed by Michel and Boy (2022), seven do have identical phases, but the remainder do not; the most discrepant have $\arg k/\arg h \approx 1.74$. None has a ratio less than 1.

5.3 Combined constraints on k_2: Results

The goal is to solve Eq. (13) for the Love number k. Even though k in (13) is not overly sensitive to the unknown "true" values of h, k', h', these values must still be assigned and an accounting made of how their uncertainties affect k. The prior values of Love numbers (those with subscript 'o') are simply those values used to produce the data of Figure 4: k_o, h_o from Wahr (1981) and k'_o, h'_o from Farrell (1972). The question is the degree of dependence on h, k', h'.

The loading numbers k', h' will be taken as real, consistent with the processing of the altimeter and SLR

Table 5 Estimates of the Love number k_2

Tide	$\lvert k_2 \rvert$	$\epsilon = -\arg k_2$	Q
Q_1	0.2983 ± 0.0010	$0.209° \pm 0.078°$	274 (190, 440)
O_1	0.2986 ± 0.0008	$0.228° \pm 0.024°$	250 (230, 275)
N_2	0.3019 ± 0.0008	$0.202° \pm 0.042°$	284 (235, 356)
M_2	0.3017 ± 0.0008	$0.178° \pm 0.020°$	322 (288, 363)

All uncertainties are 1σ.

data. New observational constraints on crustal loading from geodetic displacement measurements (Bos et al. 2015; Arnoso et al. 2023) are consistent with no significant lags in k', h', but they do imply some anelastic dispersion through adjustments in magnitude. We examined the 19 sets of loading numbers from Michel and Boy (2022) and found that the spread in the imaginary components of their k', h' lead to minimal impact on our estimate of k. However, the real parts of k', h' do have a small impact, perturbing the estimate of the phase $\epsilon = -\arg k$ by as much as about 0.02°.

In contrast, the real part of h has no significant impact on estimates of $\arg k$ but its imaginary component, or equivalently $\arg h$, does have. Varying $\arg h$ across a wide range of values between 0 and −0.5° leads to a near-linear change in the estimate of ϵ of about ±0.04°. A value of $\arg h$ near 0 is geophysically implausible if $\arg k \neq 0$, but $\arg h$ could still be small.

In summary, we examined the estimates of k from (13) over a wide range of dependencies, letting $\mathrm{Re}\, h \in [0.600, 0.625]$ and $\arg h \in [0, \arg k]$, and also letting $\mathrm{Re}\, h' \in [-0.95, -1.14]$ and $\mathrm{Re}\, k' \in [-0.305, -0.321]$; these ranges on h', k' span the differences among Farrell (1972), Martens et al. (2016), Michel and Boy (2022), and Wang et al. (2012). For M_2 the differences in estimates of $\arg k$ arising from these different constants slightly exceeded the uncertainty arising from the errors in the altimeter and tracking values of $De^{-\psi}$; for all other constituents, the reverse was true and the main uncertainty in k arose from the altimeter and tracking errors. For the magnitude $|k|$ the uncertainty in all cases was dominated by the uncertainty in h, taken conservatively as ±0.01 based on various published values, which leads to a nearly identical σ for all four constituents.

The main results for k are given in Table 5, along with the implied tidal $Q = 1/\tan\epsilon$.

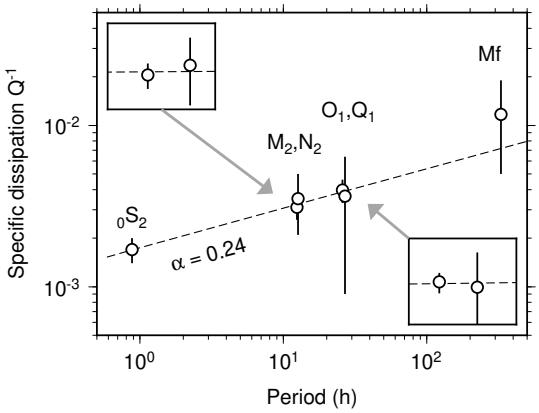

Fig. 5 Specific dissipation Q^{-1} for the four tidal constituents from Table 5, supplemented with estimates of Q^{-1} from Earth's gravest free-oscillation mode ${}_0S_2$ (Sailor and Dziewonski 1978), and from the fortnightly tide Mf (Ray and Egbert 2012). A linear fit to the ${}_0S_2$, O_1, and M_2 values gives a slope of $\alpha = 0.24$. Note these are reported geodetic Q^{-1} estimates, not adjusted to inherent mantle Q (Lau et al. 2017). Displayed error bars correspond to 2σ.

6 Discussion

A study of Earth tides is one of the few ways to determine rheological properties of the planetary interior at frequencies outside the seismic band. An important goal is then to integrate Earth-tide results with other seismic and geodetic measurements across a broad range of frequencies (e.g. Benjamin et al. 2006; Lau and Faul 2019; Ivins et al. 2020). Our new estimates of complex k_2 at both diurnal and semidiurnal frequencies bring additional independent information into that picture. Complications arise regarding how to relate attenuation in the Earth and its intrinsic Q to the tidal Q deduced from geodetic tide measurements (Efroimsky 2012; Lau et al. 2017); we need not address that here, but see Lau et al. (2017).

The estimates of tidal Q for O_1, N_2, and M_2 display a clear increase with tidal frequency. The estimate for Q_1 is slightly off that trend, but its uncertainty is so large that it spans all the values for the other three tides. Figure 5 shows our estimates of tidal Q at the two diurnal and two semidiurnal frequencies along with a higher frequency determination from the ${}_0S_2$ free-oscillation mode (Sailor and Dziewonski 1978) and a lower frequency determination from length-of-day measurements at the near-fortnightly Mf frequency (Ray and Egbert 2012). Again the main trend of increasing Q with frequency, or increasing Q^{-1} with period, holds.

The primary systematic errors in our estimates are likely to stem from complications related to violations

of lateral homogeneity, and not just the homogeneity intrinsic to the Love number formalism. We suspect that an important error source is our reliance on a constant value of seawater density, which was used to convert elevation spherical harmonics into Stokes coefficients for the analysis of orbit perturbations. Recent work with the precise laser interferometer measurements aboard the GRACE-FO satellites suggest that differences in seawater density cannot be overlooked (Han et al. 2020).

7 Summary

We have produced a new comprehensive tidal solution from three decades of laser ranging measurements to eight geodetic satellites (four satellites at the beginning of our time period; eight more recently). Results for four of the SLR-derived lunar constituents have been combined with independent tide determinations from three decades of satellite altimetry in order to arrive at new estimates of the complex Love number k_2. The Love number constraints are based on small offsets between the SLR and altimeter determinations of the degree-2 prograde spherical harmonic components. When both SLR and altimeter analyses are adjusted to use prior elastic Love numbers, k_2 and h_2, respectively, then the SLR-altimeter offsets are mainly in the quadrature component $D^+_{2m} \sin \psi^+_{2m}$ (see Figure 4) which constrain primarily the imaginary part of k_2. Results indicate that those imaginary components, which reflect dissipation in the body tide, are slightly too large in the current IERS standards for the diurnal/semidiurnal bands.

Given a complex Love number k_2, the phase lag by which the body tide lags the generating potential is given by $\epsilon = -\arg k_2$. This in turn determines the effective tidal Q. These Q estimates, for two constituents in both the diurnal and semidiurnal bands, are seen to fall along a straight line that connects previously determined Q estimates for the Earth's 54-minute free oscillation and for the fortnightly Mf tide. The slope of that line, $\alpha = 0.24$, is fairly comparable to other analyses based on a variety of seismic and geodetic measurements (cf. Benjamin et al. 2006; Ding et al. 2021).

Appendix A Atmospheric Pressure Forcing in SLR Analysis

Proper handling of atmospheric pressure data in the SLR tracking data analysis is far less critical for lunar tides than for solar tides, but it is still important and is somewhat complex. The atmosphere-ocean dealiasing models must be consistent with any explicitly modeled air-tide models.

A.1 Dealiasing model

In the development of the dealiasing models, GFZ has endeavored to remove any tidal forcing that not only would "double book" atmospheric tides but would also generate radiational ocean tides in their ocean modeling (Shihora et al. 2022). Their Release-07 product was more successful at this than their Release-06, which can be seen by examining time spectra of the model Stokes coefficients. Figure A1 gives an example for the C_{22} spherical harmonic coefficient, based on 21 years of the atmosphere-ocean time series. In Release-06 large residual peaks remain for both M_2 and S_2 tides, and these are eliminated in Release-07, although cusp energy, representing annual and other modulations, clearly remains. Curiously, Release-06 has a small peak at the frequency of the compound tide $2SM_2$; this peak does not exist in the pressure data and must have been generated by nonlinearities in the GFZ ocean model as it responded to the residual M_2 and S_2 energy; the peak is eliminated in Release-07.

Release-07 does introduce a peak at N_2 because GFZ removed any modeling of it after they noticed that the ERA5-based N_2 air pressure maps were extremely noisy. The N_2 tide is indeed very small, barely above background, but nevertheless Figure A1 suggests that the degree-2 coefficients may have been at least partly legitimate. Because of this residual N_2 peak in the dealiasing model, we have removed from our SLR analysis any explicit model for N_2 air tides, although this approach is not ideal because the energy in the dealiasing model also includes a small component that is in the ocean's response (i.e., the radiational component of the N_2 ocean tide). We also have not explicitly modeled the O_1 and Q_1 atmospheric tides; these are very small and they are difficult to extract from the generally higher background energy of the diurnal pressure band.

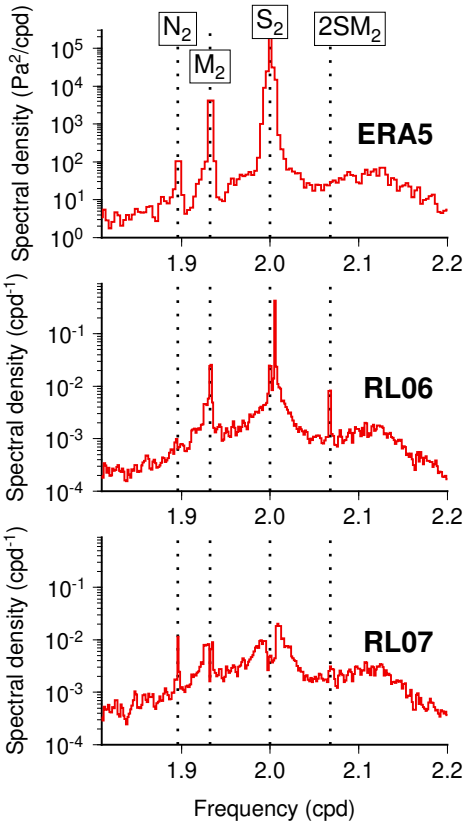

Fig. A1 Spectra of the C_{22}^{+} spherical harmonic coefficient, in the semidiurnal tidal band, of (top) ERA5 surface pressures; (middle) the GFZ atmospheric-ocean dealiasing model, Release-06 (Dobslaw et al. 2017); and (bottom) the GFZ model, Release-07 (Shihora et al. 2022). Dotted vertical lines mark frequencies of primary atmospheric tides. The tidal peaks are intended to be suppressed in the GFZ model, and Release-07 does a better job of doing that (aside from N_2). ERA5 spectra based on data from 2016–2020; GFZ spectra based on data from 2000–2020.

A.2 Air tide models

Thus, of the four lunar tides studied in this paper, we explicitly account for only the M_2 atmospheric tide in our dynamical modeling of the SLR satellites. It is included as a prior model and is based on ERA5 hourly pressures from 2006–2022. The degree-2, order-2 prograde amplitude and phase are:

$$E_{22}^{+} = 2.05\,\text{Pa}, \qquad \psi_{22}^{+} = 4.5^{\circ} \tag{A1}$$

Unfortunately, barometric tides extracted from ERA5 pressures are far from perfect. Maps of M_2 that reveal spurious trends over decades have been reported (Schindelegger and Dobslaw 2016; Ray and Schindelegger 2025). This is not unexpected, since the dynamical atmospheric models of ECMWF are ignorant of the gravitational tidal potential, so the presence of an M_2 signal must originate from data assimilation; changes in instrumentation and/or observational networks over time could then lead to false changes in the implied lunar tide. Trends can be readily seen in the degree-2 spherical harmonic components: Figure A2 shows estimates of M_2 amplitude and phase in three-year windows since 1978, and there is an obvious trend in the amplitudes which increase from 1.6 Pa to 2.2 Pa over forty years. The phases also display trend-like features in certain time intervals, but they are overall somewhat erratic. Spurious trends in the ERA5 solar tides have also been reported. In fact, spurious trends in atmospheric tides appear to be a feature of all major reanalysis products (Diaz-Argandoña et al. 2016).

The ERA5 coefficients in (A1) may be compared with two previously published empirical analyses of the M_2 tide produced from direct analysis of barometric station data. We have performed a spherical harmonic analysis of the maps produced by Schindelegger and Dobslaw (2016) and we find for the $(n, m) = (2, 2)$ amplitude and phase lag: 2.01 Pa and 12°. A much older synthesis based on considerably fewer stations was made by Haurwitz and Cowley (1969); they already computed a spherical harmonic decomposition (with different normalization) finding 1.84 Pa, 15°. The three M_2 amplitudes are not too discrepant, but the ERA5 phase lags are evidently too small. Using the Schindelegger-Dobslaw coefficients instead of ERA5 makes a small correction to the SLR tracking solution: the in-phase term is adjusted by 0.008 mm and the quadrature by −0.025 mm. This adjustment has already been applied in the foregoing analysis. It increased our estimate of tidal Q from 314 to 322, which is within the original uncertainty span.

Acknowledgments. For helpful discussions on many aspects of this work, we thank our GSFC colleagues Frank Lemoine and Nikita Zelensky. The work has been supported by the National Aeronautics and Space Administration through the Sentinel-6 and GRACE-FO projects and by the National Geospatial-Intelligence Agency (NGA). Any opinions, findings, conclusions, or recommendations expressed in this material are those of the authors and do not necessarily reflect the views of NGA, DoD, or the U.S. government. Approved for public release, NGA-U-2025-01245.

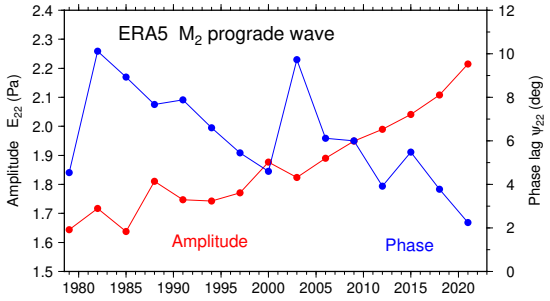

Fig. A2 Amplitudes and phase lags of the M_2 barometric tide (degree-2 prograde term) extracted in three-year windows from ERA5 surface pressures. The trends are spurious. In comparison, station barometer data imply a mean M_2 amplitude and phase lag of 2.01 Pa, 12° (Schindelegger and Dobslaw 2016), which suggests the phase in ERA5 is especially suspect.

Data Availability. Satellite laser ranging data are distributed by the NASA Crustal Dynamics Data Information System (Noll 2010), at https://www.earthdata.nasa.gov/centers/cddis-daac.

References

Agnew DC (2013) SPOTL: Some program for ocean-tide loading. SIO Tech. Rep., Scripps Institution of Oceanography, La Jolla, URL https://escholarship.org/uc/item/954322pg

Arnoso J, Bos MS, Benavent M, et al (2023) Anelastic response of the Earth's crust underneath the Canary Islands revealed from ocean tide loading observations. Geophysical Journal International 235:273–286. https://doi.org/10.1093/gji/ggad205

Benjamin D, Wahr J, Ray RD, et al (2006) Constraints on mantle anelasticity from geodetic observations, and implications for the J_2 anomaly. Geophysical Journal International 165:3–16. https://doi.org/10.1111/j.1365-246X.2006.02915.x

Bos MS, Penna NT, Baker TF (2015) Ocean tide loading displacements in western Europe: 2. GPS-observed anelastic dispersion in the asthenosphere. Journal of Geophysical Research: Solid Earth 120:6540–6557. https://doi.org/10.1002/2015JB011884

Cartwright DE, Edden AC (1973) Corrected tables of tidal harmonics. Geophysical Journal of the Royal Astronomical Society 33:253–264

Cartwright DE, Tayler RJ (1971) New computations of the tide-generating potential. Geophysical Journal of the Royal Astronomical Society 23:45–74

Cheng MK, Eanes RJ, Tapley BD (1992) Tidal deceleration of the moon's mean motion. Geophysical Journal International 108:401–409. Erratum, vol. 110, p. 218, 1992

Desai SD, Ray RD (2014) Consideration of tidal variations in the geocenter for satellite altimeter observations of ocean tides. Geophysical Research Letters 89:2454–2459. https://doi.org/10.1002/2014GL059614

Diaz-Argandoña J, Ezcurra A, Sáenz J, et al (2016) Climatology and temporal evolution of the atmospheric semidiurnal tide in present-day reanalyses. Journal of Geophysical Research: Atmospheres 121:4614–4626. https://doi.org/10.1002/2015JD024513

Ding H, Chen Z, Pan Y, et al (2021) The complex Love numbers of long-period zonal tides retreived from global GPS displacements: Applications for determining mantle anelasticity. Journal of Geophysical Research: Solid Earth 126:e2021JB022380. https://doi.org/10.1029/2021JB022380

Dobslaw H, Bergmann-Wolf I, Dill R, et al (2017) A new high-resolution model of non-tidal atmosphere and ocean mass variability for de-aliasing of satellite gravity observations: AOD1B RL06. Geophysical Journal International 211:263–269. https://doi.org/10.1093/gji/ggx302

Efroimsky M (2012) Tidal dissipation compared to seismic dissipation: In small bodies, earths, and super-earths. Astrophysical Journal 746:150. https://doi.org/10.1088/0004-637X/746/2/150

Egbert GD, Ray RD (2001) Estimates of M_2 tidal energy dissipation from Topex/Poseidon altimeter data. Journal of Geophysical Research 106:22475–22502

Farrell WE (1972) Deformation of the earth by surface loads. Reviews of Geophysics and Space Physics 10:761–797

Gill AE (1982) Atmosphere-Ocean Dynamics. Academic Press

Groten E (2004) Fundamental parameters and current best estimates of the parameters of common relevance to astronomy, geodesy, and geodynamics. Journal of Geodesy 77:724–731. https://doi.org/10.1007/s00190-003-0373-y

Han SC, Ghobadi-Far K, Ray RD, et al (2020) Tidal geopotential dependence on Earth ellipticity and seawater density and its detection with the GRACE Follow-On laser ranging interferometer. Journal of Geophysical Research: Oceans 125:e2020JC016774. https://doi.org/10.1029/2020JC016774

Hartmann T, Wenzel HG (1995) The HW95 tidal potential catalogue. Geophysical Research Letters 22:3553–3556

Haurwitz B, Cowley AD (1969) The lunar barometric tide, its global distribution and annual variation. Pure and Applied Geophysics 77:122–150

Heiskanen W, Moritz H (1967) Physical Geodesy. W. Freeman & Co.

Hersbach H, et al (2020) The ERA5 global reanalysis. Quarterly Journal of the Royal Meteorological Society 146:1999–2049. https://doi.org/10.1002/qj.3803

Ivins ER, ad S. Adhikari LC, Larour E, et al (2020) A linear viscoelasticity for decadal to centennial time scale mantle deformation. Reports on Progress in Physics 83:106801. https://doi.org/10.1088/1361-6633/aba346

Kaula WM (1962) Celestial geodesy. Advances in Geophysics 9:191–293

Kozai Y (1968) Love's number of the earth derived from satellite observations. Publ astr Soc Japan 20:24–26

Lambeck K (1977) Tidal dissipation in the oceans: Astronomical, geophysical and oceanographic consequences. Philosophical Transactions of the Royal Society 287:545–594

Lambeck K (1988) Geophysical Geodesy. Clarendon Press, Oxford

Lau HCP, Faul UH (2019) Anelasticity from seismic to tidal timescales: Theory and observations. Earth and Planetary Science Letters 508:18–29. https://doi.org/10.1016/j.epsl.2018.12.009

Lau HCP, Faul UH, Mitrovica JX, et al (2017) Anelasticity across seismic to tidal timescales: a self-consistent approach. Geophysical Journal International 208:368–384. https://doi.org/10.1093/gji/ggw401

Le Provost C (2001) Ocean tides. In: Fu LL, Cazenave A (eds) Satellite Altimetry and Earth Sciences: A Handbook of Techniques and Applications. Academic Press, San Diego, p 267–303

Loomis BD, Rachlin KE, Wiese DN, et al (2020) Replacing GRACE/GRACE-FO $C_{3,0}$ with satellite laser ranging: Impacts on Antarctic Ice Sheet mass change. Geophysical Research Letters 47:e2019GL085488. https://doi.org/10.1029/2019GL085488

Lyard F, Allain D, Cancet M, et al (2021) FES2014 global ocean tides atlas: design and performance. Ocean Science 17:615–649. https://doi.org/10.5194/os-17-615-2021

Martens HR, Rivera L, Simons M, et al (2016) The sensitivity of surface mass loading displacement response to perturbations in the elastic structure of the crust and mantle. Journal of Geophysical Research: Solid Earth 121:3911–3938. https://doi.org/10.1002/2015JB012456

Melchior P (1966) The Earth Tides. Pergamon Press, Oxford

Michel A, Boy JP (2022) Viscoelastic Love numbers and long-period geophysical effects. Geophysical Journal International 228:1191–1212. https://doi.org/10.1093/gji/ggab369

Noll CE (2010) The Crustal Dynamics Data Information System: A resource to support scientific analysis using space geodesy. Advances in Space Research 45:1421–1440. https://doi.org/10.1016/j.asr.2010.01.018

Pearlman MR, Noll CE, Pavlis EC, et al (2019) The ILRS: approaching 20 years and planning for the future. Journal of Geodesy 93:2161–2180. https://

doi.org/10.1007/s00190-019-01241-1

Petit G, Luzum B, (Eds.) (2010) IERS Conventions 2010. Tech. Note 36, International Earth Rotation and Reference Systems Service, Verlag des Bundesamts für Kartographie und Geodäsie, Frankfurt am Main

Pugh DT, Woodworth PL (2014) Sea Level Science: Understanding Tides, Surges, Tsunamis and Mean Sea-Level Changes. Cambridge Univ. Press, Cambridge

Ray RD (2013) Precise comparisons of bottom-pressure and altimetric ocean tides. Journal of Geophysical Research: Oceans 118:4570–4584. https://doi.org/10.1002/jgrc.20336

Ray RD (2025) Documentation for Goddard Ocean Tide solution GOT5: Global tides from multi-mission satellite altimetry. NASA Tech. Memo. 20250002085, Goddard Space Flight Center, Greenbelt MD

Ray RD, Egbert GD (2012) Fortnightly Earth rotation, ocean tides, and mantle anelasticity. Geophysical Journal International 189:400–413. https://doi.org/10.1111/j.1365-246X.2012.05351.x

Ray RD, Schindelegger M (2025) Trends in the M_2 ocean tide observed by satellite altimetry in the presence of systematic errors. Journal of Geodesy 99:11. https://doi.org/10.1007/s00190-025-01935-9

Ray RD, Eanes RJ, Chao BF (1996) Detection of tidal dissipation in the solid earth by satellite tracking and altimetry. Nature 381:595–597

Ray RD, Eanes RJ, Lemoine FG (2001) Constraints on energy dissipation in the earth's body tide from satellite tracking and altimetry. Geophysical Journal International 144:471–480

Rosi G, Sorrentino F, Cacciapuoti L, et al (2014) Precision measurement of the Newtonian gravitational constant using cold atoms. Nature 510:518–522. https://doi.org/10.1038/nature13433

Sailor RV, Dziewonski AM (1978) Measurements and interpretation of normal mode attenuation. Geophysical Journal of the Royal Astronomical Society 7753:559–581

Schindelegger M, Dobslaw H (2016) A global ground truth view of the lunar air pressure tide L_2. Journal of Geophysical Research: Atmospheres 121:95–110. https://doi.org/10.1002/2015JD024243

Schindelegger M, Sakazaki T, Green M (2023) Atmospheric tides—an earth system signal. In: Green M, Duarte J (eds) A Journey through Tides. Elsevier, Amsterdam, p 389–416, https://doi.org/10.1016/B978-0-323-90851-1.00007-8

Shihora L, Balidakis K, Dill R, et al (2022) Non-tidal background modeling for satellite gravimetry based on operational ECMWF and ERA5 reanalysis data: AOD1B RL07. Journal of Geophysical Research: Solid Earth 127:e2022JB024360. https://doi.org/10.1029/2022JB024360

Smith DE (1965) A determination of the even harmonics in the earth's gravitational potential function. Planetary and Space Science 13:1151–1159

Smith DE, Kolenkiewicz R, Dunn PJ (1973) Earth tidal amplitude and phase. Nature 244:498–499

Stammer D, et al (2014) Accuracy assessment of global barotropic ocean tide models. Reviews of Geophysics 52:243–282. https://doi.org/10.1002/2014RG000450

Tucker ES, Nerem RS, Loomis BD (2022) Simulation of a future SLR satellite to improve low-degree gravity estimates. Journal of Geophysical Research: Solid Earth 127:e2022JB025743. https://doi.org/10.1029/2022JB025743

Wahr JM (1981) Body tides on an elliptical, rotating, elastic and oceanless earth. Geophysical Journal of the Royal Astronomical Society 64:677–704

Wang H, Xiang L, Jia L, et al (2012) Love numbers and Green's functions for elastic Earth models PREM, iasp91, ak135, and modified models with refined crustal structure from Crust2.0. Computers and Geosciences 49:190–199. https://doi.org/10.1016/j.cageo.2012.06.022